Oxygen vacancies enhance lithium storage performance in ultralong vanadium pentoxide nanobelt cathodes

Yu, Yanlong; Li, Jinpeng; Wang, Xiaoliang; Chang, Bingdong; Wang, Jun; Ahmad, Mashkoor; Sun, Hongyu

Published in:
Journal of Colloid and Interface Science

Link to article, DOI:
10.1016/j.jcis.2018.12.046

Publication date:
2019

Document Version
Peer reviewed version

Accepted Manuscript

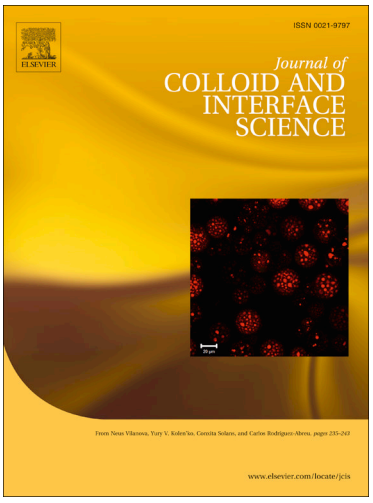

Oxygen vacancies enhance lithium storage performance in ultralong vanadium pentoxide nanobelt cathodes

Yanlong Yu, Jinpeng Li, Xiaoliang Wang, Bingdong Chang, Jun Wang, Mashkoor Ahmad, Hongyu Sun

PII: S0021-9797(18)31486-3
DOI: https://doi.org/10.1016/j.jcis.2018.12.046
Reference: YJCIS 24423

To appear in: *Journal of Colloid and Interface Science*

Received Date: 5 October 2018
Revised Date: 7 December 2018
Accepted Date: 12 December 2018

Please cite this article as: Y. Yu, J. Li, X. Wang, B. Chang, J. Wang, M. Ahmad, H. Sun, Oxygen vacancies enhance lithium storage performance in ultralong vanadium pentoxide nanobelt cathodes, *Journal of Colloid and Interface Science* (2018), doi: https://doi.org/10.1016/j.jcis.2018.12.046

Oxygen vacancies enhance lithium storage performance in ultralong vanadium pentoxide nanobelt cathodes

Yanlong Yu,[a] Jinpeng Li,[b,*] Xiaoliang Wang, [c] Bingdong Chang,[d] Jun Wang,[a] Mashkoor Ahmad,[e,*] Hongyu Sun [d,f,*]

[a] *College of chemistry and chemical engineering, Northeastern Petroleum University, Daqing 163318, PR China*

[b] *ULVAC Research Center SUZHOU Co., Ltd., Beijing 100176, PR China*

[c] *College of Science, Hebei University of Science and Technology, Shijiazhuang 050018, PR China*

[d] *DTU Danchip, Technical University of Denmark, Kongens Lyngby 2800, Denmark*

[e] *Nanomaterials Research Group (NRG), Physics Division, PINSTECH, P.O. Nilore, Islamabad 44000, Pakistan*

[f] *Department of Micro- and Nanotechnology, Technical University of Denmark, Kongens Lyngby 2800, Denmark*

* Corresponding authors. *E-mail addresses*: roclie@gmail.com (J. Li), mashkoorahmad2003@yahoo.com (M. Ahmad), hsun@nanotech.dtu.dk (H. Sun)

ABSTRACT

Ultralong V_2O_5 nanobelts have been successfully synthesized by a facile hydrothermal oxidation route. Oxygen vacancies are generated in the V_2O_5 nanobelts by annealing under N_2 atmosphere at an elevated temperature. The microstructure and chemical composition of the pristine and annealed V_2O_5 nanobelts are studied by different methods. Compared to the pristine V_2O_5 nanobelts, the annealed V_2O_5 nanobelts sample possesses a higher reversible capacity of 177.8 $mAhg^{-1}$ after 50 cycles at a current density of 0.3 Ag^{-1}, corresponding to ~0.27% capacity loss per cycle. At a higher current density of 1.2 Ag^{-1}, the reversible capacity of annealed V_2O_5 electrode can reach 128.5 $mAhg^{-1}$, which is two times larger than that of pristine V_2O_5 electrode. Ultralong flexible morphology together with oxygen vacancies in the annealed V_2O_5 electrode is considered to be responsible for the enhanced lithium storage properties.

Keywords: Vanadium pentoxide; Cathode materials; Oxygen vacancy; Ultralong nanobelts; Lithium ion batteries

1. Introduction

Lithium-ion batteries (LIBs) have been widely used in various fields as the main important energy storage devices due to their advantages of high energy density, long cycling life, and environmental benignity [1-4]. Up till now, many efforts have been made to improve the battery performance with higher energy density and longer lifetime. Usually this can be achieved by optimizing the main components in a battery system, including electrode materials, electrolyte, and separator in a specific battery structure [5-9]. It is generally accepted that the overall performance of the battery is strongly dependent on the inherent electrochemical properties of electrode materials. Most of the current commercial LIBs employ lithium cobalt oxides as cathodes, which cannot meet the requirements of high-performance LIBs due to the limited theoretical capacity, the toxicity, high cost, and safety issues of lithium cobalt oxide materials. Consequently, alternative cathodes, e.g., $LiNi_{1/3}Mn_{1/3}Co_{1/3}O_2$ [10], $LiMn_2O_4$ [11,12], and $LiMPO_4$ (M = Fe, Co, Mn, etc) [13-15], have been developed and proved to exhibit excellent lithium storage performances.

The low cost, high abundance on earth, facile synthesis, and multiple chemical valence states, the layer-structured vanadium pentoxides (V_2O_5) have attracted much attention as a promising candidate for cathodes in LIBs [16-20]. Importantly, the theoretical capacity of V_2O_5 (294 $mAhg^{-1}$ for the intercalation and deintercalation of two Li^+ ions in the potential range of 2.0 - 4.0 V is considerably higher than the conventional cathodes, including $LiFePO_4$ (170 $mAhg^{-1}$) and $LiMn_2O_4$ (148 $mAhg^{-1}$) [21,22]. However, low rate capability and poor cycling life are hindering the practical applications of V_2O_5 cathode materials, which mainly come from the intrinsic low electrical conductivity and sluggish charge diffusion during cycling. A wide range of methods have been developed to solve the issues and to improve the lithium storage properties of V_2O_5 materials. For example, design and synthesis of micro- and nanostructures of V_2O_5 cathodes with optimized size, morphology, composition, and assembly can facilitate the efficient mass and charge transportations, and accommodate the volume changes during cycling [23-26]; combining V_2O_5 electrodes with carbon nanotubes, graphene, or conducting polymers can improve the electrical conductivity and modify the chemical

properties on the interface between electrode and electrolyte [19,27-31].

Defect engineering is a robust route to modify material behaviors and different physical/chemical properties [32-34]. Recently, this strategy has also been employed to anodes and cathodes for rechargeable batteries to improve the capacity, durability, or rate capability [35-37]. Taking metal oxide-based electrode materials as an example, the existence of oxygen vacancies leads to the delocalization of electron distribution and promotion of electron excitation, which are favorable for the conductivity improvement and charge transportation. In our previous works, facile approaches have been developed to controllably generate oxygen vacancies in metal oxide-based anodes, including laser irradiation treatment and chemical reduction in solution [38,39]. The results show that an optimized oxygen deficiency is important to achieve well-balanced electronic/ionic transport and thus boost the ion storage. The role of oxygen vacancies in electrochemical transitions has been studied for conventional cathode materials ($LiNi_{1/3}Mn_{1/3}Co_{1/3}O_2$, $LiMn_2O_4$, and $LiMPO_4$) [40-42], and superior lithium storage properties of those cathode materials can be achieved by controlling the formation and distribution of oxygen vacancies. Nevertheless, less attention has been paid to investigate the oxygen vacancy engineering in V_2O_5 cathodes and their electrochemical properties [43].

In this work, we synthesize ultralong V_2O_5 nanobelts by using a facile hydrothermal oxidation method. The obtained V_2O_5 nanobelts are subjected to anneal in N_2 atmosphere at elevated temperature. It is demonstrated that oxygen vacancies are generated in the annealed sample while the belt-like morphology and crystalline structure are preserved upon the thermal treatment, which are favorable for improving lithium storage properties.

2. Experimental details

2.1 Materials synthesis

V_2O_5 powder and hydrogen peroxide solution (H_2O_2, 30 wt%) were purchased from Sinopharm Chemical Regent Co. Ltd. Ultralong V_2O_5 nanobelts were synthesized by a facile hydrothermal oxidation reaction. In a typical process, V_2O_5 powder (0.455 g) and deionized

water (37.5 mL) were mixed under vigorous magnetic stirring at room temperature, and then H_2O_2 (6.25 mL) was added and kept continuously stirred for 30 min. Finally a transparent orange solution was obtained. The resultant solution was transferred to a Teflon lined autoclave (50 mL) and kept in an oven at 205 ^oC for 3 days. The product was washed with anhydrous ethanol and deionized water several times. The sample was dried at 80 ^oC in vacuum for 6 h and then annealed at 400 ^oC for 1 h in N_2 atmosphere. The as prepared samples and the annealed ones are denoted as p-V_2O_5 and a-V_2O_5 respectively.

2.2 Materials characterization

The morphology and chemical composition of the samples were studied by employing field-emission scanning electron microscopy (FESEM; Hitachi-S5500, 5 keV) equipped with an energy dispersive X-ray (EDX) system, and transmission electron microscopy (TEM; FEI, Tecnai G^2 20, 200 keV; JEOL, JEM-2011, 200 keV). The surface composition and valence-state were determined by X-ray photoelectron spectroscopy (XPS, Thermo Fisher 250XI), and the results were calibrated by referencing C1s at 284.6 eV. Crystallographic and phase information were acquired by using a Bruker Model D8 Advance X-ray powder diffractometer (XRD) with Cu-K_α irradiation (λ=1.5418 Å).

2.3 Electrochemical measurements

The working electrode slurry was prepared by dispersing V_2O_5 samples, carbon black and poly(vinylidene fluoride) (PVDF) binder in N-methylpyrrolidone with a weight ratio of 70:20:10. The slurry was spread on aluminum foil disks and dried in a vacuum oven at 120 ^oC overnight prior to Swagelok-type cell assembly. Lithium foil was used as the counter and reference electrode, and 1.0 M $LiPF_6$ in ethyl carbonate/dimethyl carbonate (1:1 v/v ratio) was used as the electrolyte. Cyclic voltammetry (CV; 2.0-4.0 V, 0.2 mV s^{-1}) measurements were performed on a CHI660C electrochemical workstation. Galvanostatic charging/discharging tests were conducted at a constant current density of 0.3 A g^{-1}. Rate performance was conducted at various current densities of 0.3, 0.6, 0.9, 1.2, and 0.3 A g^{-1}, each for 10 cycles. The electrochemical impedance spectroscopy (EIS) measurements were collected at open

circuit voltage on an electrochemical impedance analyzer (Solartron 1260 + 1287). The frequency rang was 1 mHz - 100 kHz, and the amplification voltage was10 mV.

3. Results and Discussion

The initial ultralong V_2O_5 nanobelts (p-V_2O_5) were synthesized by a simple H_2O_2 assisted hydrothermal reaction process. To form oxygen vacancies in the V_2O_5 nanobelts, the products were annealed in N_2 atmosphere at an elevated temperature (a-V_2O_5). The crystallographic structure and phase purity of the samples were determined by XRD as shown in Fig. 1. For p-V_2O_5 sample (black pattern in Fig. 1), all diffraction peaks match well with the standard pattern of the orthorhombic-phase V_2O_5 (blue pattern in Fig. 1, JCPDS No. 41-1426). No additional diffraction peaks are detected, suggesting a high phase purity of the samples. After thermal annealing, the a-V_2O_5 sample (red pattern in Fig. 1) shows similar diffraction patterns compared with that of p-V_2O_5 sample. No obvious changes of peak positions and intensities are observed in both samples, indicating the employed annealing does not alter the phase structure and crystallite size of V_2O_5 sample.

The morphology of the samples was characterized by FESEM as shown in Fig. 2. Low and high magnification FESEM images of p-V_2O_5 sample (Fig. 2a, b) confirm the large scale synthesis of ultralong nanobelts with smooth surface. The length is in the order of several hundred micrometers, and the width is ranging from 20 to 40 nm. Typical EDX result shows only the existence of O and V elements in the sample, and quantitative analysis gives an average V to O atomic ratio of 30:70 (Fig. 2c), which is close to the theoretical value of 2:5. After thermal annealing at 400 ^oC in N_2 atmosphere, the morphology of the nanobelts became more loosen, with a more dispersive width distribution ranging from 10 nm to 50 nm (Fig. 2d, e). Quantitative EDX analysis indicates that the average atomic ratio of V/O in a-V_2O_5 sample is 33:67 (Fig. 2f) suggesting the presence of oxygen deficiency in a-V_2O_5 nanobelts compared with p-V_2O_5 nanobelts. This can be further confirmed by XPS analysis as we will discuss below. Related results have also been reported in other metal oxides that are annealed in inert atmospheres.

More detailed structure characterizations of the p-V_2O_5 and a-V_2O_5 nanobelts were performed by TEM. Fig. 3a and b show typical TEM images of p-V_2O_5 nanobelt bundles and a single p-V_2O_5 nanobelt, which again confirm the thin and ultralong nanobelt morphology with a smooth surface. The lattice-resolved high resolution TEM (HRTEM) image taken from the edge of a single nanobelt (Fig. 3b) is shown in Fig. 3c. The interplanar distance of fringes is measured to be ~0.58 nm, which corresponds to the spacing of the (200) plane of orthorhombic-phase V_2O_5 (see the schematic illustration in Fig. 3d). Fast Fourier transform (FFT) is also performed as shown in the inset of Fig. 3c, and the FFT pattern is found to be identical to the entire part of the nanobelt, indicating the single crystalline nature of the ultralong V_2O_5 nanobelt. For the a-V_2O_5 samples, the belt-like morphology is preserved after the annealing treatment and the layer structure extends along the nanobelts (Fig. 3e-g). The d-spacing of annealed sample measured from HRTEM image is ~0.58 nm (Fig. 3h), which is the same as the pristine sample, further indicating no significant change of V_2O_5 crystal structure after N_2 thermal treatment. It should be noticed that the crystalline quality on the nanobelt edge (Fig. 3g) is poorer than the center part (Fig. 3h), which may be attributed to the electron beam induced structural degradation during the TEM imaging [44].

XPS analysis was employed to study the change of surface electronic states and chemical composition for p-V_2O_5 and a-V_2O_5 nanobelts (with an average depth of ~5 nm). Fig. 4a and b show high-resolution XPS spectra of the V 2p regions. There is no obvious change in all peak positions of spectra. The binding energies of V $2p_{1/2}$ and V $2p_{3/2}$ for a-V_2O_5 and p-V_2O_5 were ~525.4 eV and ~517.9 eV, respectively. The values are in good agreement with previously reported results [29]. Fig. 4c and d show the deconvoluted peaks of the O 1s regions by Gaussian–Lorentzian fitting after subtracting a linear background from the raw data. It is found that the O 1s peak of p-V_2O_5 nanobelts (Fig. 4d) can be best fitted by three components located at ~529.1, 530.8, and 531.9 eV. Those peaks are attributed to oxygen atoms in the lattice (O_L), -OH group related species (or oxygen vacancies O_V), and oxygen atoms in water molecule absorbed on the sample surfaces (O_W) [45]. In contrast, two peaks corresponding to O_L and O_V can be fitted to O 1s spectrum for a-V_2O_5 sample (Fig. 4c). The disappearance of

O_W peak can be attributed to the annealing treatment at elevated temperature. The relative intensity ratio of O_V/O_L of a-V_2O_5 (0.428) is higher than that of p-V_2O_5 (0.254), further indicating oxygen vacancies are generated by the annealing in N_2 atmospheres.

The ultralong belt-like morphology and modified surface electronic states in a-V_2O_5 samples can provide more active sites and facilitate more efficient mass diffusion and ion transport, thus good lithium storage properties can be expected. The electrochemical properties of a-V_2O_5 and p-V_2O_5 samples were firstly studied by CV between 2.0 and 4.0 V (vs. Li^+/Li) at a scan rate of 0.2 mV s^{-1}. The representative CV curves are shown in Fig. 5, implying similar electrochemical characteristics for both samples. In the first cycle, three evident reduction peaks located at 3.3, 3.1, and 2.2 V are observed, indicating multistep reduction processes that correspond to the successive phase transformations from α-V_2O_5 to ε-$Li_{0.5}V_2O_5$, ε-$Li_{0.5}V_2O_5$ to δ-LiV_2O_5, and δ-LiV_2O_5 to γ-$Li_2V_2O_5$, respectively. The following oxidation peaks at 2.5, 2.6, 3.3, and 3.5 V are ascribed to the Li deintercalation and the successive backward phase transformation. In the subsequent cycles, the CV curves are almost identical to the first cycle, indicating the gradual stabilization of V_2O_5 electrodes after the first cycle and good reversibility during the electrochemical reactions. The above processes can be summarized by the following equations [46]:

$$\alpha\text{-}V_2O_5 + 0.5Li^+ + 0.5e^- \leftrightarrow \varepsilon\text{-}Li_{0.5}V_2O_5 \quad (1)$$

$$\varepsilon\text{-}Li_{0.5}V_2O_5 + 0.5Li^+ + 0.5e^- \leftrightarrow \delta\text{-}LiV_2O_5 \quad (2)$$

$$\delta\text{-}LiV_2O_5 + 1Li^+ + 0.5e^- \leftrightarrow \gamma\text{-}Li_2V_2O_5 \quad (3)$$

Besides the main redox peaks mentioned above, it is also interesting to find that there is a pair of minor redox peaks appearing ~3.57, 3.67 V and a shoulder peak located at 3.3 V in a-V_2O_5 sample, while these peaks are suppressed in p-V_2O_5 sample. The additional redox peaks are associated with some structural changes, and the split peak might result from the introduction of oxygen vacancies in a-V_2O_5. Similar results have also been reported in metal (V [47] and Cu [48]) doped V_2O_5 nanostructures and V_2O_5/C@MWCNTs nanohybrid cathodes [49].

Fig. 6a and b show galvanostatic discharge and charge curves of a-V_2O_5 and p-V_2O_5 electrodes in the first three cycles, which were evaluated at a current density of 0.3 Ag^{-1}. The

discharge and charge processes show multiple redox plateaus in the studied potential window of 2.0 – 4.0 V, demonstrating the successive structural transformation (reactions (1)-(3)), which is in agreement with the CV analysis. The first discharge and charge capacities are 206.4 and 189.9 $mAhg^{-1}$ for the a-V_2O_5 electrode, while 209.2 and 234.3 $mAhg^{-1}$ for p-V_2O_5 electrode. In the subsequent cycles, the reversible capacities decrease and stabilize at 188 and 197 $mAhg^{-1}$ for a-V_2O_5 and p-V_2O_5 electrodes, respectively. Although the reversible capacity of a-V_2O_5 is slightly lower than p-V_2O_5 in the first three cycles, it shows better stability in the cycling test. Fig. 6c shows the comparison of cycling performance between the a-V_2O_5 and p-V_2O_5 electrodes at a current density of 0.3 Ag^{-1} up to 50 cycles. In the first nine cycles, the capacities obviously decrease. For example, for the electrodes of a-V_2O_5 and p-V_2O_5, the reversible capacities decrease from 205 and 208.1 to 179.8 and 183.6 $mAhg^{-1}$. After 10 cycles, the capacity of p-V_2O_5 continuously decreases, while the a-V_2O_5 electrode shows a much more stable capacity. The initial capacity fading is related to the structural change of V_2O_5 electrodes during cycling, which results in the reduction of the available active sites for lithium storage and thus increased electron polarization [50]. For a-V_2O_5 electrode with oxygen vacancies, the microstructures adjust dynamically that allows the activation of lithium ion diffusion [38]. Therefore, the a-V_2O_5 electrode shows a higher capacity than that of p-V_2O_5 electrode after the initial several cycles. The reversible capacities are 177.8 and 164.4 $mAhg^{-1}$ after 50 cycles for a-V_2O_5 and p-V_2O_5 electrodes, corresponding to 86.7% and 79% of the initial capacities and about 0.27% and 0.42% capacity loss per cycle. Conclusively, the a-V_2O_5 electrode exhibits not only a higher capacity, but also a better cycling performance than the p-V_2O_5 electrode. The rate capabilities of the two electrodes evaluated at different current densities are presented in Fig. 6d and e. When the current density increases from 0.3 to 1.2 Ag^{-1}, the capacities of p-V_2O_5 electrode decrease rapidly from 175.6 to 64.4 $mAhg^{-1}$, while the a-V_2O_5 electrode delivers higher capacities at the same current densities. Especially at the highest current density of 1.2 Ag^{-1}, the reversible capacity of a-V_2O_5 electrode can reach 128.5 $mAhg^{-1}$, which is two times larger than that of p-V_2O_5 electrode. When the current density is settled back to 0.3 Ag^{-1}, the reversible capacity can be regained to the initial

values. The results above demonstrate a superior rate performance of a-V_2O_5 electrodes compared with p-V_2O_5 electrodes in the studied current density range, especially at higher current densities. The better rate performance of a-V_2O_5 electrode is associated with oxygen vacancies, which can enhance the conductivity of the active materials, and accelerate the ion diffusion even at a high current density [38,39].

The reversible capacity and rate capability of the present ultralong belt-like a-V_2O_5 electrode is found to be higher than that of commercial V_2O_5 powder or nanoparticles (75 $mAhg^{-1}$ @0.17 A g^{-1} [51], 58 $mAhg^{-1}$ @0.1 A g^{-1} [52]), indicating the unique advantage of the one-dimensional electrode morphology. However, it should be mentioned here that the absolute specific capacity of a-V_2O_5 electrodes is inferior to other reported V_2O_5 cathodes with controlled complex morphology, assembly, or chemical composition [53,54]. To quantitatively compare the effect of electrode treatments on lithium storage properties, we define a parameter $r(i)$, which equals to the ratio of reversible capacity of modified V_2O_5 electrodes via different strategies (morphology, assembly, composition, or defect engineering) to the pristine ones at a given current density of i. For example, the r(1.2 A g^{-1}) value of oxygen vacancy engineering is 200% (128.5/64.4). This value is obvious higher than that of controlling morphology, assembly, or composition, such as yolk-shelled V_2O_5 microspheres (140%, 0.3 A g^{-1}) [16], V_2O_5@carbon nanotubes (176%, 0.3 A g^{-1}) [19], V_2O_5 nanowires and reduced graphene oxide composites (150%, 0.6 A g^{-1}) [46], V doped V_2O_5 nanoflakes (127%, 1.0 A g^{-1}) [47], and Cu doped V_2O_5 flowers (157%, 0.9 A g^{-1}) [48]. Our results highlight the potential applications of the oxygen vacancy engineering in improving the electrochemical performance of V_2O_5 cathodes. It is anticipated that better lithium storage properties can be achieved in the V_2O_5 cathodes with oxygen vacancies by combining the existing strategies together.

Fig. 6f displays the Nyquist plots of a-V_2O_5 and p-V_2O_5 electrodes after 50 cycling tests. The plots consist of an intercept at high-frequency, a semicircle diameter, and a linear plot in low-frequency range, which are associated with the electrical resistance of the electrolyte (R_e), the charge-transfer resistance (R_{ct}), and the Li^+ ion diffusion in the electrodes (Warburg

impedance, Z_w), respectively [53]. The components can be determined by modeling AC impendence spectra using an equivalent circuit as shown in the inset of Fig. 6f. It is found that the simulated R_{ct} value for a-V_2O_5 electrode (81 Ω) is smaller than that for p-V_2O_5 electrode (117 Ω), indicating a more efficient transportation of lithium ions and a more sufficient utilization of the electrode in the a-V_2O_5 sample. In addition, the morphology of the a-V_2O_5 and p-V_2O_5 electrodes was investigated by TEM as shown in Fig. 7. Both samples maintain the initial belt-like morphology, demonstrating the stability during cycling test.

Based on the above results, the improved lithium storage properties of a-V_2O_5 can be attributed to the synergistic effects of ultralong flexible morphology and oxygen vacancies generation by the annealing treatment. First, the existence of oxygen vacancies improves the intrinsic conductivity and facilitates the efficient usage of each active nanostructure, which can improve the charge transportation and thus the rate performance. Second, ultralong nanobelts provide enough space to accommodate the local volume change upon charge/discharge cycling, thus improving the cycling stability. Third, the nanobelts with one-dimensional morphology possess more active sites to store lithium ions, increasing the specific capacity in the active materials.

4. Conclusions

In this work, we report a facile method to synthesize and modify ultralong V_2O_5 nanobelts by a hydrothermal oxidation method and subsequent thermal annealing in N_2 atmosphere. Structure and composition characterizations show that oxygen vacancies are generated after the heat treatment. The ultralong flexible morphology and oxygen vacancies improve the intrinsic conductivity and facilitate an efficient usage of each active nanostructure. When evaluated as cathode materials for LIBs, the a-V_2O_5 sample shows better lithium storage properties compared to the p-V_2O_5 sample. Specifically, the a-V_2O_5 nanobelts possess a reversible capacity of 177.8 $mAhg^{-1}$ after 50 cycles at a current density of 0.3 Ag^{-1}. At a higher current density of 1.2 Ag^{-1}, a reversible capacity of 128.5 $mAhg^{-1}$ can be achieved. We anticipate that the lithium storage properties of the ultralong V_2O_5 nanobelt electrodes can

be further improved by optimizing annealing conditions and combining other strategies, such as morphology and composition engineering that have been explored before.

Acknowledgments

This work was supported by National Natural Science Foundation of China (No. 51401114, 51601037, 51701063), and Young Talents Program in University of Hebei Province (BJ2018014).

References

[1] M. Armand, J.-M. Tarascon, Building better batteries, Nature 451 (2008) 652–657. doi:10.1038/451652a.

[2] B. Scrosati, J. Hassoun, Y.-K. Sun, Lithium-ion batteries: a look into the future, Energy Environ. Sci. 4 (2011) 3287. doi:10.1039/c1ee01388b.

[3] J.B. Goodenough, K.-S. Park, The Li-ion rechargeable battery: a perspective, J. Am. Chem. Soc. 135 (2013) 1167–1176. doi:10.1021/ja3091438.

[4] H.D. Yoo, E. Markevich, G. Salitra, D. Sharon, D. Aurbach, On the challenge of developing advanced technologies for electrochemical energy storage and conversion, Mater. Today 17 (2014) 110–121. doi:10.1016/J.MATTOD.2014.02.014.

[5] H. Wu, Y. Cui, Designing nanostructured Si anodes for high energy lithium ion batteries, Nano Today 7 (2012) 414–429. doi:10.1016/J.NANTOD.2012.08.004.

[6] S.-T. Myung, K. Amine, Y.-K. Sun, Nanostructured cathode materials for rechargeable lithium batteries, J. Power Sources 283 (2015) 219–236. doi:10.1016/J.JPOWSOUR.2015.02.119.

[7] L. Dai, D.W. Chang, J.-B. Baek, W. Lu, Carbon nanomaterials for advanced energy

conversion and storage, Small 8 (2012) 1130–1166. doi:10.1002/smll.201101594.

[8] M.D. Bhatt, C. O'Dwyer, Recent progress in theoretical and computational investigations of Li-ion battery materials and electrolytes, Phys. Chem. Chem. Phys. 17 (2015) 4799–4844. doi:10.1039/C4CP05552G.

[9] M. Armand, F. Endres, D.R. MacFarlane, H. Ohno, B. Scrosati, Ionic-liquid materials for the electrochemical challenges of the future, Nat. Mater. 8 (2009) 621–629. doi:10.1038/nmat2448.

[10] T. Ohzuku, Y. Makimura, Layered lithium insertion material of $LiCo_{1/3}Ni_{1/3}Mn_{1/3}O_2$ for lithium-ion batteries, Chem. Lett. 30 (2001) 642–643. doi:10.1246/cl.2001.642.

[11] T. Ohzuku, M. Kitagawa, T. Hirai, Electrochemistry of manganese dioxide in lithium nonaqueous cell, J. Electrochem. Soc. 136 (1989) 3169. doi:10.1149/1.2096421.

[12] D. Aurbach, M.. Levi, K. Gamulski, B. Markovsky, G. Salitra, E. Levi, U. Heider, L. Heider, R. Oesten, Capacity fading of $Li_xMn_2O_4$ spinel electrodes studied by XRD and electroanalytical techniques, J. Power Sources 81–82 (1999) 472–479. doi:10.1016/S0378-7753(99)00204-9.

[13] A.K. Padhi, K.S. Nanjundaswamy, J.B. Goodenough, Phospho-olivines as positive-electrode materials for rechargeable lithium batteries, J. Electrochem. Soc. 144 (1997) 1188. doi:10.1149/1.1837571.

[14] H. Wang, Y. Yang, Y. Liang, L.-F. Cui, H. Sanchez Casalongue, Y. Li, G. Hong, Y. Cui, H. Dai, $LiMn_{1-x}Fe_xPO_4$ nanorods grown on graphene sheets for ultrahigh-rate-performance lithium ion batteries, Angew. Chemie. Int. Ed. 50 (2011) 7364–7368. doi:10.1002/anie.201103163.

[15] J. Ni, L. Zhang, S. Fu, S.V. Savilov, S.M. Aldoshin, L. Lu, A review on integrating

nano-carbons into polyanion phosphates and silicates for rechargeable lithium batteries, Carbon 92 (2015) 15–25. doi:10.1016/J.CARBON.2015.02.047.

[16] A. Pan, H. B. Wu, L. Yu, X.W. Lou, Template-free synthesis of VO_2 hollow microspheres with various interiors and their conversion into V_2O_5 for lithium-ion batteries, Angew. Chemie Int. Ed. 52 (2013) 2226–2230. doi:10.1002/anie.201209535.

[17] Y. Li, J. Yao, E. Uchaker, J. Yang, Y. Huang, M. Zhang, G. Cao, Leaf-like V_2O_5 nanosheets fabricated by a facile green approach as high energy cathode material for lithium-ion batteries, Adv. Energy Mater. 3 (2013) 1171–1175. doi:10.1002/aenm.201300188.

[18] L. Mai, Q. An, Q. Wei, J. Fei, P. Zhang, X. Xu, Y. Zhao, M. Yan, W. Wen, L. Xu, Nanoflakes-assembled three-dimensional hollow-porous V_2O_5 as lithium storage cathodes with high-rate capacity, Small 10 (2014) 3032–3037. doi:10.1002/smll.201302991.

[19] D. Kong, X. Li, Y. Zhang, X. Hai, B. Wang, X. Qiu, Q. Song, Q.-H. Yang, L. Zhi, Encapsulating V_2O_5 into carbon nanotubes enables the synthesis of flexible high-performance lithium ion batteries, Energy Environ. Sci. 9 (2016) 906–911. doi:10.1039/C5EE03345D.

[20] H. Wang, X. Bi, Y. Bai, C. Wu, S. Gu, S. Chen, F. Wu, K. Amine, J. Lu, Open-structured $V_2O_5{\cdot}nH_2O$ nanoflakes as highly reversible cathode material for monovalent and multivalent intercalation batteries, Adv. Energy Mater. 7 (2017) 1602720. doi:10.1002/aenm.201602720.

[21] X.-L. Wu, L.-Y. Jiang, F.-F. Cao, Y.-G. Guo, L.-J. Wan, $LiFePO_4$ nanoparticles embedded in a nanoporous carbon matrix: superior cathode material for electrochemical energy-storage devices, Adv. Mater. 21 (2009) 2710–2714. doi:10.1002/adma.200802998.

[22] D.K. Kim, P. Muralidharan, H.-W. Lee, R. Ruffo, Y. Yang, C.K. Chan, H. Peng, R.A. Huggins, Y. Cui, Spinel $LiMn_2O_4$ nanorods as lithium ion battery cathodes, Nano Lett. 8 (2008)

3948–3952. doi:10.1021/nl8024328.

[23] Z. Li, G. Liu, M. Guo, L.-X. Ding, S. Wang, H. Wang, Electrospun porous vanadium pentoxide nanotubes as a high-performance cathode material for lithium-ion batteries, Electrochim. Acta 173 (2015) 131–138. doi:10.1016/J.ELECTACTA.2015.05.057.

[24] Q. An, P. Zhang, F. Xiong, Q. Wei, J. Sheng, Q. Wang, L. Mai, Three-dimensional porous V_2O_5 hierarchical octahedrons with adjustable pore architectures for long-life lithium batteries, Nano Res. 8 (2015) 481–490. doi:10.1007/s12274-014-0638-1.

[25] X. Rui, Y. Tang, O.I. Malyi, A. Gusak, Y. Zhang, Z. Niu, H.T. Tan, C. Persson, X. Chen, Z. Chen, Q. Yan, Ambient dissolution–recrystallization towards large-scale preparation of V_2O_5 nanobelts for high-energy battery applications, Nano Energy 22 (2016) 583–593. doi:10.1016/J.NANOEN.2016.03.001.

[26] X. Ren, Y. Zhai, L. Zhu, Y. He, A. Li, C. Guo, L. Xu, Fabrication of various V_2O_5 hollow microspheres as excellent cathode for lithium storage and the application in full cells, ACS Appl. Mater. Interfaces 8 (2016) 17205–17211. doi:10.1021/acsami.6b03257.

[27] M. Ihsan, Q. Meng, L. Li, D. Li, H. Wang, K.H. Seng, Z. Chen, S.J. Kennedy, Z. Guo, H.-K. Liu, V_2O_5/mesoporous carbon composite as a cathode material for lithium-ion batteries, Electrochim. Acta 173 (2015) 172–177. doi:10.1016/J.ELECTACTA.2015.05.060.

[28] X. Yao, G. Guo, P.-Z. Li, Z.-Z. Luo, Q. Yan, Y. Zhao, Scalable synthesis of honeycomblike V_2O_5/carbon nanotube networks as enhanced cathodes for lithium-ion batteries, ACS Appl. Mater. Interfaces 9 (2017) 42438–42443. doi:10.1021/acsami.7b15136.

[29] Y. Yang, L. Li, H. Fei, Z. Peng, G. Ruan, J.M. Tour, Graphene nanoribbon/V_2O_5 cathodes in lithium-ion batteries, ACS Appl. Mater. Interfaces 6 (2014) 9590–9594.

doi:10.1021/am501969m.

[30] Y. Zhang, Y. Wang, Z. Xiong, Y. Hu, W. Song, Q. Huang, X. Cheng, L.-Q. Chen, C. Sun, H. Gu, V_2O_5 nanowire composite paper as a high-performance lithium-ion battery cathode, ACS Omega 2 (2017) 793–799. doi:10.1021/acsomega.7b00037.

[31] J.H. Lee, J.-M. Kim, J.-H. Kim, Y.-R. Jang, J.A. Kim, S.-H. Yeon, S.-Y. Lee, Toward ultrahigh-capacity V_2O_5 lithium-ion battery cathodes via one-pot synthetic route from precursors to electrode sheets, Adv. Mater. Interfaces 3 (2016) 1600173. doi:10.1002/admi.201600173.

[32] J. Nowotny, M.A. Alim, T. Bak, M.A. Idris, M. Ionescu, K. Prince, M.Z. Sahdan, K. Sopian, M.A. Mat Teridi, W. Sigmund, Defect chemistry and defect engineering of TiO_2-based semiconductors for solar energy conversion, Chem. Soc. Rev. 44 (2015) 8424–8442. doi:10.1039/C4CS00469H.

[33] W. Jia, Y. Wu, Y. Chen, D. He, J. Li, Y. Wang, Z. Wang, W. Zhu, C. Chen, Q. Peng, D. Wang, Y. Li, Interface-induced formation of onion-like alloy nanocrystals by defects engineering, Nano Res. 9 (2016) 584–592. doi:10.1007/s12274-016-0999-8.

[34] Y. Wang, L.-T. Tseng, P.P. Murmu, N. Bao, J. Kennedy, M. Ionesc, J. Ding, K. Suzuki, S. Li, J. Yi, Defects engineering induced room temperature ferromagnetism in transition metal doped MoS_2, Mater. Des. 121 (2017) 77–84. doi:10.1016/J.MATDES.2017.02.037.

[35] Y.S. Yun, V.-D. Le, H. Kim, S.-J. Chang, S.J. Baek, S. Park, B.H. Kim, Y.-H. Kim, K. Kang, H.-J. Jin, Effects of sulfur doping on graphene-based nanosheets for use as anode materials in lithium-ion batteries, J. Power Sources 262 (2014) 79–85. doi:10.1016/J.JPOWSOUR.2014.03.084.

[36] J. Liu, R. Jiang, X. Wang, T. Huang, A. Yu, The defect chemistry of $LiFePO_4$ prepared by hydrothermal method at different pH values, J. Power Sources 194 (2009) 536–540. doi:10.1016/J.JPOWSOUR.2009.05.007.

[37] K. Hoang, Defect physics, delithiation mechanism, and electronic and ionic conduction in layered lithium manganese oxide cathode materials, Phys. Rev. Appl. 3 (2015) 024013. doi:10.1103/PhysRevApplied.3.024013.

[38] H. Wan, Y. Liu, H. Zhang, W. Zhang, N. Jiang, Z. Wang, S. Luo, H. Arandiyan, H. Liu, H. Sun, Improved lithium storage properties of Co_3O_4 nanoparticles via laser irradiation treatment, Electrochim. Acta 281 (2018) 31–38. doi:10.1016/J.ELECTACTA.2018.05.156.

[39] H. Sun, Y. Zhao, K. Mølhave, M. Zhang, J. Zhang, Simultaneous modulation of surface composition, oxygen vacancies and assembly in hierarchical Co_3O_4 mesoporous nanostructures for lithium storage and electrocatalytic oxygen evolution, Nanoscale 9 (2017) 14431–14441. doi:10.1039/C7NR03810K.

[40] R. Amin, J. Maier, Effect of annealing on transport properties of $LiFePO_4$: towards a defect chemical model, Solid State Ionics 178 (2008) 1831–1836. doi:10.1016/J.SSI.2007.11.017.

[41] X. Hao, X. Lin, W. Lu, B.M. Bartlett, Oxygen vacancies lead to loss of domain order, particle fracture, and rapid capacity fade in lithium manganospinel ($LiMn_2O_4$) batteries, ACS Appl. Mater. Interfaces 6 (2014) 10849–10857. doi:10.1021/am500671e.

[42] P.K. Nayak, E.M. Erickson, F. Schipper, T.R. Penki, N. Munichandraiah, P. Adelhelm, H. Sclar, F. Amalraj, B. Markovsky, D. Aurbach, Review on challenges and recent advances in the electrochemical performance of high capacity Li- and Mn-rich cathode materials for Li-ion batteries, Adv. Energy Mater. 8 (2018) 1702397. doi:10.1002/aenm.201702397.

[43] X. Peng, X. Zhang, L. Wang, L. Hu, S.H.-S. Cheng, C. Huang, B. Gao, F. Ma, K. Huo, P.K. Chu, Hydrogenated V_2O_5 nanosheets for superior lithium storage properties, Adv. Funct. Mater. 26 (2016) 784–791. doi:10.1002/adfm.201503859.

[44] D.S. Su, M. Wieske, E. Beckmann, A. Blume, G. Mestl, R. Schlögl, Electron beam induced reduction of V_2O_5 studied by analytical electron microscopy, Catal. Letters. 75 (2001) 81–86. doi:10.1023/A:1016754922933.

[45] Z. Li, G. Liu, M. Guo, L.-X. Ding, S. Wang, H. Wang, Electrospun porous vanadium pentoxide nanotubes as a high-performance cathode material for lithium-ion batteries, Electrochim. Acta 173 (2015) 131–138. doi:10.1016/J.ELECTACTA.2015.05.057.

[46] D. Pham-Cong, K. Ahn, S.W. Hong, S.Y. Jeong, J.H. Choi, C.H. Doh, J.S. Jin, E.D. Jeong, C.R. Cho, Cathodic performance of V_2O_5 nanowires and reduced graphene oxide composites for lithium ion batteries, Curr. Appl. Phys. 14 (2014) 215–221. doi:10.1016/J.CAP.2013.10.022.

[47] H. Q. Song, C. F. Liu, C. K. Zhang, G. Z. Cao, Self-doped V^{4+}–V_2O_5 nanoflake for 2 Li-ion intercalation with enhanced rate and cycling performance, Nano Energy 22 (2016) 1–10. http://dx.doi.org/10.1016/j.nanoen.2016.02.004.

[48] H. Yu, X. H. Rui, H. T. Tan, J. Chen, X. Huang, C. Xu, W. L. Liu, D. Y. W. Yu, H. H. Hng, H. E. Hosterb, Q. Y. Yan, Cu doped V_2O_5 flowers as cathode material for high-performance lithium ion batteries, Nanoscale 5 (2013) 4937–4943. doi: 10.1039/c3nr00548h.

[49] Y. D. Liu, G. H. Gao, X. Liang, G. M. Wu, Nanofibers of V_2O_5/C@MWCNTs as the cathode material for lithium-ion batteries, J. Solid State Electrochem. 22 (2018) 2385–2393. https://doi.org/10.1007/s10008-018-3952-9.

[50] F. Maroni, A. Birrozzi, G. Carbonari, F. Croce, R. Tossici, S. Passerini, F. Nobili, Graphene/V_2O_5 cryogel composite as a high-energy cathode material for lithium-ion batteries, ChemElectroChem 4 (2017) 613–619. doi: 10.1002/celc.201600798.

[51] P. Kumar, F. Wu, T. Chou, L.H. Hu, Chemically modified morphologies of vanadium pentoxide as superior cathode material for lithium ion battery, J. Alloys Compd. 632 (2015) 126–132. http://dx.doi.org/10.1016/j.jallcom.2015.01.174.

[52] G.Z. Li, Y.C. Qiu, Y. Hou, H.F. Li, L.S. Zhou, H. Deng, Y.G. Zhang, Synthesis of V_2O_5 hierarchical structures for long cycle-life lithium-ion storage, J. Mater. Chem. A, 3 (2015) 1103–1109. doi: 10.1039/c4ta04864d.

[53] Y. Yue, H. Liang, Micro- and nano-structured vanadium pentoxide (V_2O_5) for electrodes of lithium-ion batteries, Adv. Energy Mater. 7 (2017) 1602545. doi:10.1002/aenm.201602545.

[54] H. Wang, D. Ma, Y. Huang, X. Zhang, Electrospun V_2O_5 nanostructures with controllable morphology as high-performance cathode materials for lithium-ion batteries, Chem. - A Eur. J. 18 (2012) 8987–8993. doi:10.1002/chem.201200434.

Figures captions

Fig. 1. XRD patterns of pristine V_2O_5 nanobelts (p-V_2O_5, black) and annealed V_2O_5 nanobelts treated by N_2 at 400 ^oC (a-V_2O_5, red). The standard diffraction of orthorhombic-phase V_2O_5 is also shown for comparison (JCPDS No. 41-1426, blue).

Fig. 2. (a, d) Low-, (b, e) high- magnification FESEM images, and (c, f) EDX analysis of V_2O_5 samples: (a-c) p-V_2O_5 nanobelts; (d-f) a-V_2O_5 nanobelts.

Fig. 3. TEM and HRTEM images of V_2O_5 samples: (a-c) p-V_2O_5 nanobelts; (e-h) a-V_2O_5 nanobelts; (d) crystal structure of orthorhombic-phase V_2O_5; insets of c, d are the FFT patterns of the HRTEM images.

Fig. 4. High-resolution XPS spectra of (a, c) a-V_2O_5 and (b, d) p-V_2O_5 samples (a, b) V 2p region, (c, d) O 1s region.

Fig. 5. CV curves of (a) a-V_2O_5 and (b) p-V_2O_5 electrodes of the first three cycles. The potential window and scan rate are 2.0 - 4.0 V (vs. Li^+/Li) and 0.2 mVs^{-1}, respectively.

Fig. 6. Galvanostatic charge/discharge curves of (a) a-V_2O_5 and (b) p-V_2O_5 electrodes for the first three cycles. The potential window and current density are 2.0 - 4.0 V (vs. Li^+/Li) and 0.3 A g^{-1}, respectively. (c) Comparison of the cycling performance of p-V_2O_5 (black) and a-V_2O_5 (red) electrodes for 50 cycles; Rate capability of (d) a-V_2O_5 and (e) p-V_2O_5 electrodes at different current densities between 0.3 A g^{-1} and 1.2 A g^{-1}; (f) EIS Nyquist plot of the p-V_2O_5 (black) and a-V_2O_5 (red) electrodes after 50 discharge/charge cycles. The raw impedance data can be best fitted with the inset equivalent electrical circuit, where R_e is the electrolyte resistance, R_{ct} is the charge-transfer resistance, Z_w is the Warburg impedance, and CPE is the constant phase-angle element, respectively.

Fig. 7. TEM images of (a) a-V_2O_5 and (b) p-V_2O_5 electrodes after 50 discharge/charge cycles.

Graphical Abstract

Annealing in N_2 atmosphere allows for the generation of oxygen vacancies in ultralong V_2O_5 nanobelts, which show improved lithium storage properties compared to the pristine V_2O_5 nanobelts.